Rare Metal Materials and Engineering
Volume 50, Issue 6, June 2021
Available online at www.rmme.ac.cn

Science Press

Cite this article as: Li Huiming, Zhang Jingli, Mao Xiaonan, et al. Hot Deformation Behavior and Constitutive Models of Ti600 Alloy in (α+β) Phase Region[J]. Rare Metal Materials and Engineering, 2021, 50(06): 1980-1989.

ARTICLE

Hot Deformation Behavior and Constitutive Models of Ti600 Alloy in (α+β) Phase Region

Li Huiming[1,2], Zhang Jingli[2], Mao Xiaonan[2], Hong Quan[2], Zhang Yongqiang[2], Pan Hao[2], Cai Jianhua[2]

[1] Northeastern University, Shenyang 110819, China; [2] Northwest Institute for Nonferrous Metal Research, Xi'an 710016, China

Abstract: The high-temperature deformation behavior of Ti600 alloy with a lamellar initial microstructure was investigated in the temperature range of 800~960 ℃ and the strain rate range of 10^{-3}~1 s^{-1}. Subsequently, the strain hardening exponent (n) was proposed to characterize the competition of flow softening and work hardening. The softening behavior of this alloy was also studied according to flow curve analysis and microstructure observation. The results indicate that deformation parameters have significant influences on the flow behavior of Ti600 alloy. The n-value gradually decreases after the peak strain, which indicates that the dynamic softening begins to take dominant. The dynamic softening behavior of Ti600 alloy mainly attributes to the bending, fragmentation, dynamic recovery and recrystallization of α phase during the high-temperature deformation according to the microstructure characterization. Based on experimental data, original strain-compensated Arrhenius, Hensel-Spittel and modified Arrhenius constitutive models are established to describe the deformation behavior of Ti600 alloy. The flow stresses predicted by three models are compared with experimental results, and the calculated correlation coefficients are 0.965, 0.989, and 0.997. Also, the values of average absolute relative error are 12.86%, 9.74%, and 3.26%. These results suggest that three models can descript the flow behavior of Ti600 alloy, and the modified Arrhenius model exhibits the highest prediction accuracy.

Key words: Ti600 alloy; hot compression; deformation behavior; softening behavior; constitutive models

The thermal-mechanical processes of metals are often complicated due to the deformation parameters such as temperature, strain rate, and strain[1,2]. The final mechanical properties of workpieces are not only determined by the initial microstructural state, but also closely related to the hot working process. The hot deformation of metals is often accompanied by the competition of work hardening (WH) and dynamic softening which mainly includes dynamic recovery (DRV) and dynamic recrystallization (DRX) [3,4]. Therefore, modelling high-temperature deformation behavior and understanding microstructure evolution of metals are critical to optimize thermoforming parameters and to fabricate high-quality workpieces[5].

In recent years, researchers have carried out many experimental studies on the hot deformation of metals, and established various models to characterize the hot deformation behavior. Cai et al[6] researched the high-temperature deformation of 3Cr23Ni8Mn3N heat-resistant steel and proposed a strain-compensated Arrhenius equation based on the influence of deformation strain on flow stress to forecast the hot deformation stress. Long et al[7] used genetic algorithms to calculate the material parameters of strain-compensated Arrhenius model, and established optimized Arrhenius model. Wang et al[8] combined iterative method with regression analysis to obtain material constants in the Arrhenius model. Hence, the Arrhenius constitutive model was widely used for characterizing hot deformation features of metals. Also, similar Arrhenius equations were established to predict deformation characteristics of titanium alloys[9-11], aluminum alloys[12-14], magnesium alloys[15-17], Ni-based alloys[18-20], and steel[21-23]. Under various deformation conditions, the microstructure evolution of metals is generally different. Researchers usually combine the microstructure evolution with flow behavior to establish constitutive models with physical

Received date: June 04, 2020
Foundation item: National Natural Science Foundation of China (51805442)
Corresponding author: Zhang Jingli, Ph. D., Northwest Institute for Nonferrous Metal Research, Xi'an 710016, P. R. China, Tel: 0086-29-86250729, E-mail: zhangjingli2018@163.com

meaning. Based on the theory of dislocation density, Bobbili et al[24] proposed a physically-based constitutive model, and brought this model and dynamic recrystallization kinetic into the ABAQUS finite element software to successfully predict the hot deformation behavior of Ti-10V-2Fe-3Al alloy. Haghdadi et al[25] improved the E-M model to characterize the WH and DRV of LDX 2101 duplex steel. In addition, various types of models such as K-H-L[26], J-C[27] and F-B[28] have also been proposed to depict the flow behavior of metals. Artificial neural network[29] is the model established through computer analysis, which is more and more popular in industrial production due to its efficiency and convenience. It is mainly used to predict the hot deformation behavior of metals, establish hot processing maps, and model process-structure-performance relationships[30].

The above models can be roughly classified into three types: phenomenological models[31], physically-based models[32] and artificial intelligence models[33]. Among them, phenomenological models only require conventional mathematical calculations rather than complex physical parameters. They are more efficient, and the prediction accuracy can also be achieved. Therefore, phenomenological models are commonly applied in practical researches.

Owing to the excellent comprehensive properties, such as high temperature tensile strength, superior creep performance and great fatigue resistance, Ti600 alloy has always been considered as the candidate material applied in aerospace engine parts. The aerospace engine has always been employed under the high-temperature or high-pressure environment, which requires excellent mechanical properties. The mechanical performance of the metal is largely linked to its deformation process, and the workpieces with great comprehensive performance can be obtained by reasonable processing techniques.

In this work, the hot deformation tests were conducted on Ti600 alloy, and its deformation behavior was investigated within a wide range of deformation temperatures (800~960 °C) and strain rates (10^{-3}~1 s^{-1}). Based on experimentally obtained flow curves, original strain-compensated Arrhenius model (OSCA), Hensel-Spittel model (HS) and modified Arrhenius model (MA) were introduced to depict the deformation behavior of Ti600 alloy. Additionally, the estimated accuracy of the three models was also quantitatively evaluated.

1 Experiment

The alloy used in this experiment was the forged Ti600 alloy with a chemical composition of Ti-6Al-2.8Sn-4Zr-0.4Mo-0.4Si-0.1Y (wt%). The β transus temperature was determined to be 1010±5 °C through the metallographic method. The initial microstructure of studied alloy was a typical lamellar microstructure. The thermal compression experiment was performed on a Gleeble-3800 thermal-mechanical simulation, and the compressive temperatures were 800~960 °C , and strain rates were 10^{-3}~1 s^{-1}. The specimens for hot compression experiment were cylinders of Φ8 mm×12 mm. Fig.1 shows a schematic diagram illustrating the experimental procedure of hot deformation. Before hot compression, the samples were firstly heated up to the preset temperature at the heating rate of 10 °C/s and kept for 5 min to ensure a uniform temperature distribution. After that, the samples were compressed to a true strain of 0.916, followed by immediately quenching in order to obtain hot deformation microstructure. Subsequently, the quenched samples were sliced along the direction parallel to compression axis. After grinding, polishing, and etching (10 mL HF+30 mL HNO_3+60 mL H_2O), the deformed microstructures were observed through OLYMPUSPM3 optical microscope (OM).

2 Hot Deformation Results and Discussion

2.1 Flow curves of hot deformation

Fig. 2 shows the flow curves of Ti600 alloy after hot compression over the deformation temperatures of 800~960 °C and the strain rates of 10^{-3}~1 s^{-1}. It clearly shows that all stress curves exhibit the continuous softening behavior, in which no steady-state stress appears after the peak stress because of the insufficient softening. And it also can be seen from Fig. 2 that the deformation parameters have prominent effects on flow stress. The peak stress decreases with the reduction of strain rates and the elevation of temperatures, which is consistent with other titanium alloys. During the hot deformation, a great deal of dislocation is generated within the deformed alloy at the initial work hardening stage. Subsequently, the dislocation entanglement and pileup occur, which cause the rapid increase of flow stress. It is worth mentioning that the rapid increase of dislocation content will lead to a higher stress level at the high strain rate. With further deformation, the flow curve begins to soften, which results in a decrease of work hardening rate. During this stage, dislocation rearrangement and climb are carried out as a result of the DRV, which lead to the decrease of dislocation density. When the DRV is difficult to overcome the WH and the deformation activation energy reaches a critical level, the DRX process is activated within the alloy. Subsequently, grain boundary migration consumes a large amount of dislocation, and the true stress continues to decline. Besides, at the lower

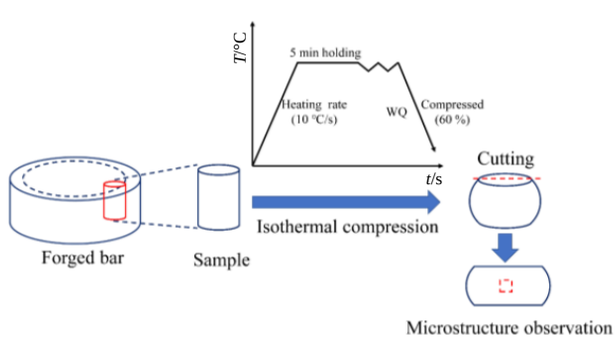

Fig.1 Schematic depiction for specimen preparation, isothermal compression and microstructure observation

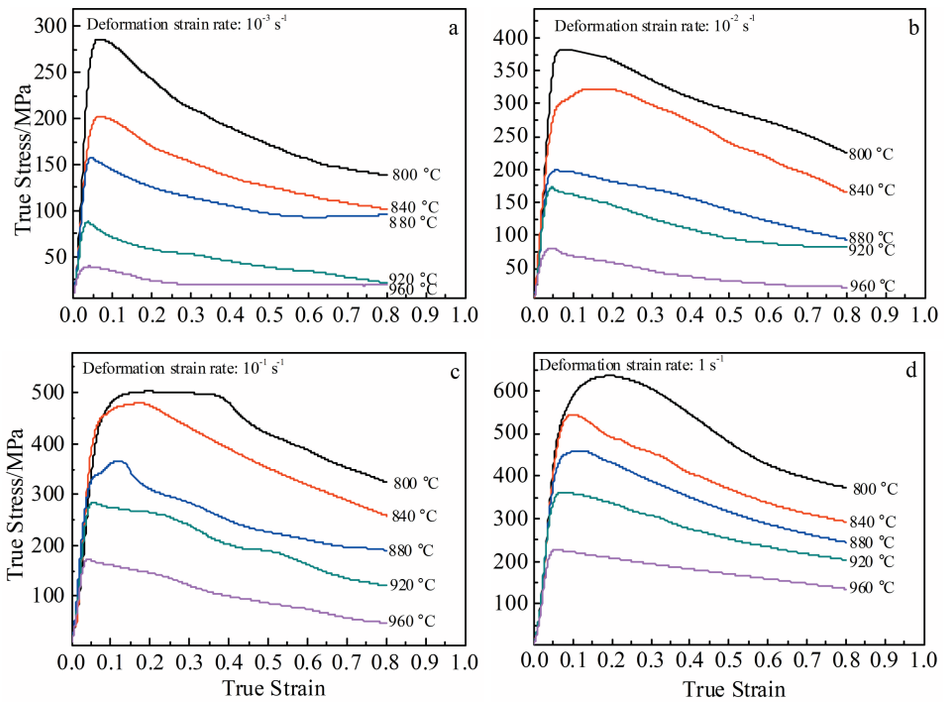

Fig.2 Flow curves of Ti600 alloy at different temperatures and strain rates: (a) 10^{-3} s^{-1}, (b) 10^{-2} s^{-1}, (c) 10^{-1} s^{-1}, and (d) 1 s^{-1}

strain rate, the deformed alloy has longer residence time at the high temperature, that is to say, it has sufficient time to release the distortion energy which can promote the softening process. Therefore, the DRV and DRX are responsible for the flow softening of Ti600 alloy during high-temperature deformation according to flow curves.

2.2 Softening behavior

The competitive relationship between dynamic softening and work hardening can be reflected by the strain hardening exponent (n) [34] during the hot deformation. The n-values calculated by Eq. (1) are shown in Fig. 3. As the strain increases, most n-values gradually decrease under different deformation conditions. The dynamic softening and work hardening reach the balance at the peak strain, and the n-value is zero at this time. With the continuous increase of deformation strain, the dynamic softening begins to dominate, causing a decreased n-value. It can be noted that n-value shows a linear decrease when the strain rate increases to 1 s^{-1} by comparing the variation of n-value at different strain rates. This can be explained that the dislocation density inside deformed grain is high at the high strain rate, and a large amount of dislocation must be eliminated in subsequent softening process, which makes the n-value decrease rapidly. Moreover, the rapidly decreased n-value also reveals that the softening rate is faster at the high strain rate. For α+β titanium alloy, the close-packed hexagonal structure α phase is believed to have fewer slip systems than β phase which is the body-centered cubic structure and is hard to deform. The α phase is often termed as strengthening phase in α+β titanium alloy[35]. Therefore, the strain hardening exponent and softening behavior are significantly affected by the microstructure evolution of α phase during hot deformation. The strain hardening exponent can be expressed as:

$$n = \left.\frac{\mathrm{d}\lg\sigma}{\mathrm{d}\lg\varepsilon}\right|_{\dot{\varepsilon},T} \tag{1}$$

where σ is the true stress (MPa), ε is the strain, $\dot{\varepsilon}$ is the strain rate (s^{-1}) and T is the absolute temperature (K).

According to microstructure characterization, the deformation behavior of studied alloy can be understood more distinctly. Fig.4 displays the thermal compression microstructures of Ti600 alloy at 880~960 °C and 10^{-3}~10^{-1} s^{-1}. It is evident that the original grain boundaries of equiaxed β are broken and disappear, and the lamellar α phase structure is retained. Owing to the compression deformation, the lamellar α phase is elongated along the direction perpendicular to the compression direction, as shown in Fig.4b. Fig.4c includes the deformed α phase, fragmentized α phase, and recrystallized α phase, which indicate that the non-uniform deformation occurs at the deformation temperature of 920 °C and strain rate of 10^{-3} s^{-1}. During the compression deformation process, the grain boundaries deform firstly due to the anisotropy of grain boundaries. A large number of dislocations are formed at the grain boundaries, and these generated dislocations can promote the formation of sub-grains. The Ti600 alloy belongs to high stacking fault energy metal for a high Al content. For high stacking fault energy metal, continuous dynamic recrystallization is prone to occur during hot deformation[36]. This means that dislocations will be consumed by the formation of

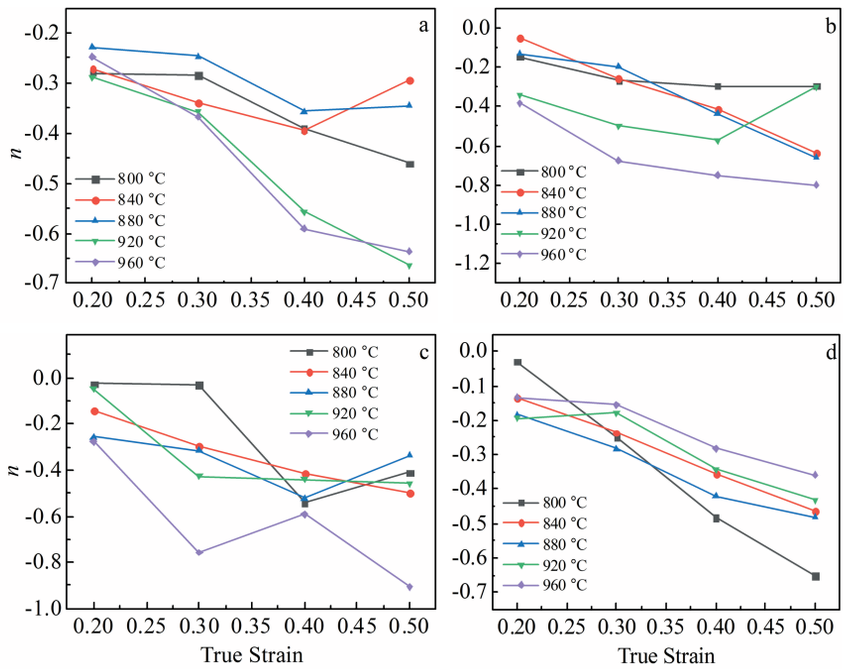

Fig.3 Variation of strain hardening exponent (n) at diffident strain rates: (a) 10^{-3} s^{-1}, (b) 10^{-2} s^{-1}, (c) 10^{-1} s^{-1}, and (d) 1 s^{-1}

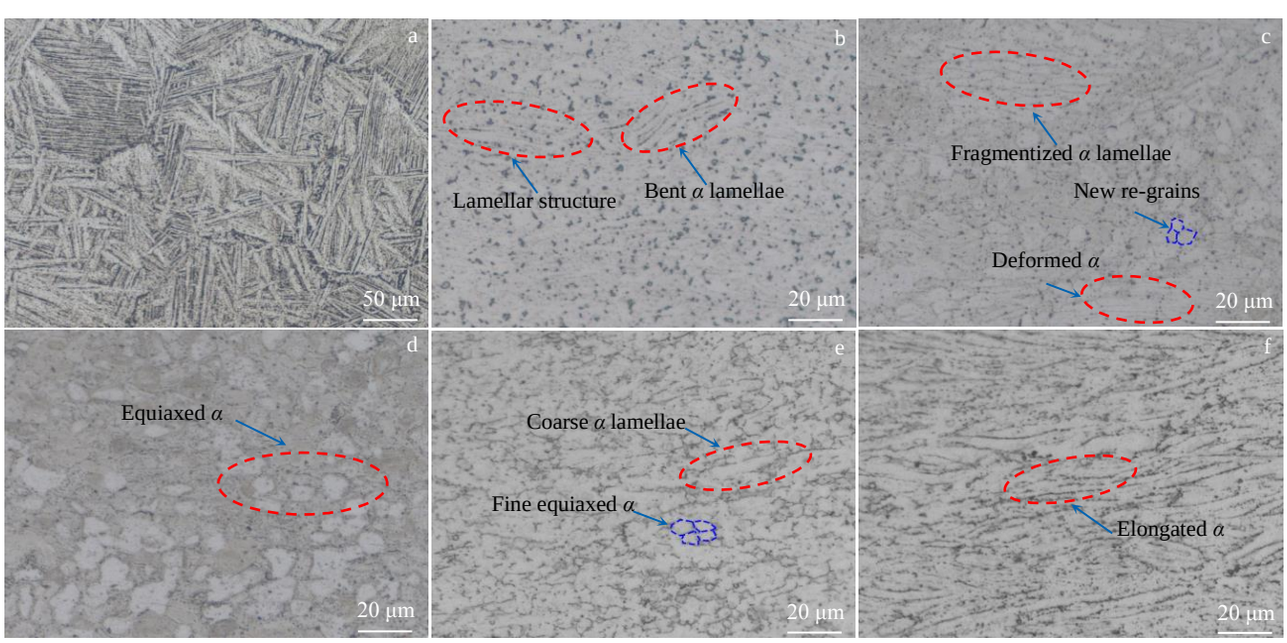

Fig.4 Microstructures of Ti600 alloy after the hot deformation under different conditions: (a) initial structure, (b) 880 °C/10^{-3} s^{-1}, (c) 920 °C/10^{-3} s^{-1}, (d) 960 °C/10^{-3} s^{-1}, (e) 960 °C/10^{-2} s^{-1}, (f) 960 °C/10^{-1} s^{-1}

sub-grains and low-angle grain boundaries will eventually be transformed into high-angle grain boundaries. Therefore, the DRX process occurs firstly at the grain boundaries. With the further deformation, local strain occurs in lamellar structure within the grains, which may become the second nucleation site for DRX. And the lamellar structure with soft orientation is easier to undergo DRX than the hard-oriented lamellae. When the alloy is deformed at 960 °C and 10^{-3} s^{-1}, sufficient DRX takes place and all original structures are replaced by recrystallized grains (re-grains). In addition, full DRX can

lead to the refinement of initial microstructure of Ti600 alloy (Fig.4d).

Under the deformation temperature of 960 ℃, the elongated α lamellae along the metal flow direction can be readily observed as the strain rate increases to 10^{-1} s^{-1} (Fig.4f). At this time, there is a higher dislocation density in the deformed microstructure. When the strain rate decreases from 10^{-1} s^{-1} to 10^{-2} s^{-1}, some fine equiaxed α grains appear in the microstructure, which indicate that insufficient DRX occurs (Fig.4e). When the strain rate reaches to 10^{-3} s^{-1}, the re-grains grow slightly because the longer time contributes to the coarsening of re-grains during hot compression, as shown in Fig.4d. Hence, the softening behavior of Ti600 alloy during high-temperature deformation is mainly induced by the bending, fragmentation, DRV and DRX of α phase.

3 Constitutive Models and Discussion

The constitutive model is mainly applied to evaluate the flow behavior of alloys during the hot deformation, to calculate the deformation parameters, and to provide a theoretical basis for the finite element numerical simulation[37]. The thermoplastic deformation of titanium alloy is a thermally activated process, which includes the WH, DRV and DRX processes. In this study, three kinds of constitutive models including original strain-compensated Arrhenius (OSCA), Hensel-Spittel (HS) and modified Arrhenius (MA) model are conducted to predict the flow behavior of Ti600 alloy. And the prediction accuracy of three models is also evaluated.

3.1 Original strain-compensated Arrhenius (OSCA) model

Sellars and Tagart[38] did lots of pioneering works on the hot deformation, and proposed the Arrhenius equation to describe the flow stress of metals. The equations are as follows:

$$\dot{\varepsilon} = AF(\sigma)\exp\left(\frac{-Q}{RT}\right) \tag{2}$$

$$F(\sigma) = \begin{cases} \sigma^{n_1} & \alpha\sigma < 0.8 \\ \exp(\beta\sigma) & \alpha\sigma > 1.2 \\ [\sinh(\alpha\sigma)]^n & \text{for all } \sigma \end{cases} \tag{3}$$

where $\dot{\varepsilon}$ represents the strain rate (s^{-1}); σ is the flow stress (MPa); A, α, β are material constants; n_1, n are flow stress exponents and $\alpha=\beta/n_1$; Q represents the activation energy of high-temperature deformation (kJ/mol); R is the gas constant (8.314 J/mol/K), and T is the absolute temperature (K).

Eq.(4) shows the equation of Zener-Hollomon parameter[39] which is considered to evaluate the dependence of the deformation behavior on the deformation parameters during high-temperature deformation. Eq.(2) and Eq.(3) are substituted into Eq.(4), and the flow stress can be described by Eq.(5).

$$Z = \dot{\varepsilon}\exp\left(\frac{Q}{RT}\right) = A[\sinh(\alpha\sigma)]^n \tag{4}$$

$$\sigma = \frac{1}{\alpha}\ln\left\{\left(\frac{Z}{A}\right)^{1/n} + \left[\left(\frac{Z}{A}\right)^{2/n} + 1\right]^{1/2}\right\} \tag{5}$$

However, it can be found that the deformation strain has a significant influence on the flow stress of Ti600 alloy through observing the flow curves. To correct the effect of strain and to improve the prediction accuracy, all material constants are calculated by above Eq.(2) and Eq.(4) with an interval of 0.05 within the strain range of 0.1~0.75. Fig.5 shows the variation of material constants at different strains. The relationships between material constants and strains can be determined by the polynomial fitting, and the fitted results are listed in Table 1. Finally, all material constants can be obtained by following equations.

$$\begin{cases} \alpha(\varepsilon) = B_0 + B_1\varepsilon + B_2\varepsilon^2 + B_3\varepsilon^3 + B_4\varepsilon^4 + B_5\varepsilon^5 \\ n(\varepsilon) = C_0 + C_1\varepsilon + C_2\varepsilon^2 + C_3\varepsilon^3 + C_4\varepsilon^4 + C_5\varepsilon^5 \\ Q(\varepsilon) = D_0 + D_1\varepsilon + D_2\varepsilon^2 + D_3\varepsilon^3 + D_4\varepsilon^4 + D_5\varepsilon^5 + D_6\varepsilon^6 + D_7\varepsilon^7 \\ \ln A(\varepsilon) = E_0 + E_1\varepsilon + E_2\varepsilon^2 + E_3\varepsilon^3 + E_4\varepsilon^4 + E_5\varepsilon^5 + E_6\varepsilon^6 + E_7\varepsilon^7 \end{cases} \tag{6}$$

Substituting the material constants obtained by above fitted polynomial equations into Eq.(5), the flow stresses of Ti600 alloy under all experimental conditions can be determined. So as to evaluate the accuracy of this constitutive model, the stresses calculated by the strain-compensated Arrhenius equation are compared with the measured stresses. Fig.6 shows the contrast of flow stresses obtained by OSCA model with the experimental results. It can be observed from Fig.6 that the OSCA model can predict the flow stress of Ti600 alloy. And a similar trend exists between measured and predicted flow stress. However, under some deformation conditions, the predicted results have some differences compared to the experimental stresses, and the differences are positive or negative. It can be explained that the model only considers the effect of strain when calculating the material constants, whose average values are used under the same strain at various deformation conditions, whereas ignores the influences of deformation temperatures and strain rates.

3.2 Hensel-Spittel (HS) model

Hensel and Spittel[40] explored another constitutive equation to depict the flow stress of metals. HS model considers the effects of strain, deformation temperature, and strain rate, and this model can be written as:

$$\sinh(\alpha\sigma) = A\exp(m_1T)\varepsilon^{m_2}\dot{\varepsilon}^{m_3}\exp(m_4/\varepsilon)\times (1+\varepsilon)^{m_5T}\exp(m_6\varepsilon)\dot{\varepsilon}^{m_7T}T^{m_8} \tag{7}$$

where m_1, m_2, m_3, m_4, m_5, m_6, m_7 and m_8 are material coefficients. To simplify the calculation, m_7 and m_8 are generally ignored. The α value can be computed by above fitted polynomial.

Taking logarithm of Eq.(7), the stress can be expressed as Eq.(8). Substituting experimental data into Eq.(8), a mathematical software is used to perform multiple linear regression analysis. Subsequently, the material coefficients are given in Table 2. The predicted stresses and experimental stresses are compared to verify the accuracy of HS model (Fig.7). Note that the overall stress difference is small, but under some particular conditions such as low temperatures (800 and 840 ℃), the gap of the predicted flow stress and the experimental stress is large.

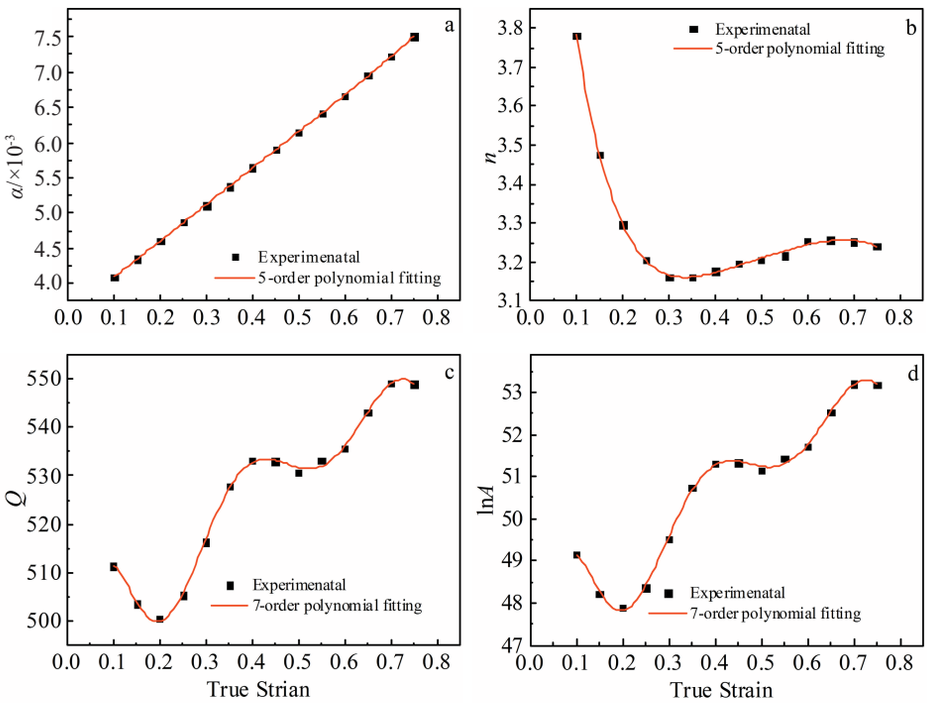

Fig.5 Variation of material constants at different true strains: (a) α, (b) n, (c) Q, and (d) ln$A$

Table 1 Coefficients of the fitted polynomial

α	n	Q	ln$A$
B_0=0.00364	C_0=5.012	D_0=366.766	E_0=35.424
B_1=0.00426	C_1=-17.811	D_1=4356.999	E_1=424.281
B_2=0.00432	C_2=66.221	D_2=-48611.427	E_2=-4810.435
B_3=-0.00865	C_3=-120.662	D_3=255861.498	E_3=25468.258
B_4=0.00682	C_4=110.779	D_4=-706232.32	E_4=-70367.298
B_5=-0.00108	C_5=-41.338	D_5=1.056×10^6	E_5=105077.191
		D_6=-810173.70	E_6=-80367.249
		D_7=249823.776	E_7=24677.067

$$\ln\sinh(\alpha\sigma) = \ln A + m_1 T + m_2 \ln\varepsilon + m_3 \ln\dot{\varepsilon} + m_4/\varepsilon + m_5 T\ln(1+\varepsilon) + m_6\varepsilon \quad (8)$$

3.3 Modified Arrhenius (MA) model

The OSCA model only considers the single influence of strain, deformation temperatures and strain rates on material constants, in which the flow stress cannot be accurately predicted under some experimental conditions. A modified Arrhenius model, considering multiple effects of the thermodynamic parameters, is expressed as:

$$\dot{\varepsilon} = A(\varepsilon,\dot{\varepsilon},T)\left[\sinh(\alpha(\varepsilon,T)\sigma)\right]^{n(\varepsilon,T)}\exp\left(\frac{-Q(\varepsilon,\dot{\varepsilon},T)}{RT}\right) \quad (9)$$

Taking logarithm of Eq.(9), Eq.(10) can be defined as:

$$\ln\dot{\varepsilon} = \ln A(\varepsilon,\dot{\varepsilon},T) + n(\varepsilon,T)\left[\sinh(\alpha(\varepsilon,T)\sigma)\right] - \frac{Q(\varepsilon,\dot{\varepsilon},T)}{RT} \quad (10)$$

Material constants in Eq. (10) can be determined by following equations:

$$\alpha(\varepsilon,T) = \left[\frac{\partial\ln\dot{\varepsilon}}{\partial\sigma(\varepsilon,T)}\right] \Big/ \left[\frac{\partial\ln\dot{\varepsilon}}{\partial\ln\sigma(\varepsilon,T)}\right] \quad (11)$$

$$n(\varepsilon,T) = \left\{\frac{\partial\ln\dot{\varepsilon}}{\partial\ln\left[\sinh(\alpha(\varepsilon,T)\sigma)\right]}\right\}_{\varepsilon,T} \quad (12)$$

$$Q(\varepsilon,\dot{\varepsilon},T) = R\left\{\frac{\partial\ln\dot{\varepsilon}}{\partial\ln\left[\sinh(\alpha(\varepsilon,T)\sigma)\right]}\right\}_{\varepsilon,T}\left\{\frac{\partial\ln\left[\sinh(\alpha(\varepsilon,T)\sigma)\right]}{\partial(1/T)}\right\}_{\varepsilon,\dot{\varepsilon}} = Rn(\varepsilon,T)n_3(\varepsilon,\dot{\varepsilon}) \quad (13)$$

Eq.(10) also can be transformed as Eq.(14):

$$\ln A(\varepsilon,\dot{\varepsilon},T) = \frac{Q(\varepsilon,\dot{\varepsilon},T)}{RT} + \ln\dot{\varepsilon} - n(\varepsilon,T)\left[\sinh(\alpha(\varepsilon,T)\sigma)\right] = n(\varepsilon,T)n_3(\varepsilon,\dot{\varepsilon})/T + S(\varepsilon,T) \quad (14)$$

The values of α, n, and n_3 under different experimental conditions can be calculated by above equations, and the results are shown in Fig.8. Subsequently, the results are fitted by binary polynomial, and the fitted equation is Eq.(15). The coefficients of polynomial are shown in Table 3, and the values of material constants can be obtained through Eq.(15).

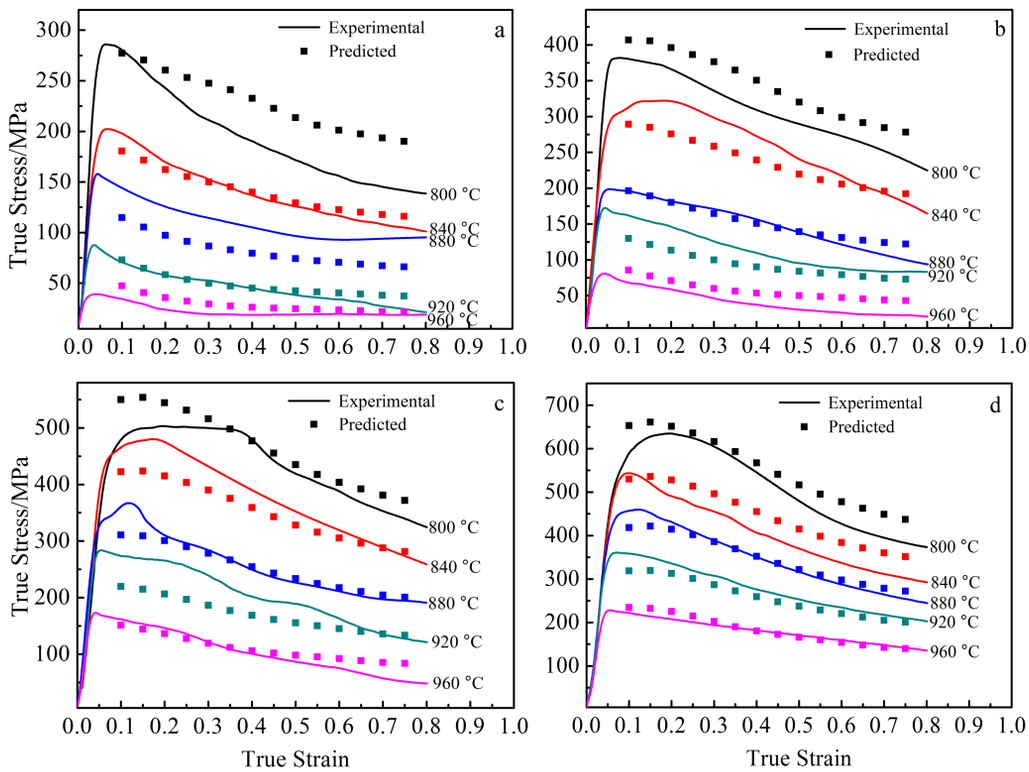

Fig.6 Comparison between the predicted stresses by OSCA model and experimental stresses: (a) 10^{-3} s^{-1}, (b) 10^{-2} s^{-1}, (c) 10^{-1} s^{-1}, and (d) 1 s^{-1}

Table 2 Material coefficients in HS model

A	m_1	m_2	m_3	m_4	m_5	m_6
277451.105	-0.0124	-0.149	0.289	-0.0623	-0.0058	3.458

Fig. 9 shows the deviation between predicted stresses and experimental stresses of MA model. It can be seen that all precited stresses are consistent with measured stresses, and the MA model shows the higher accuracy.

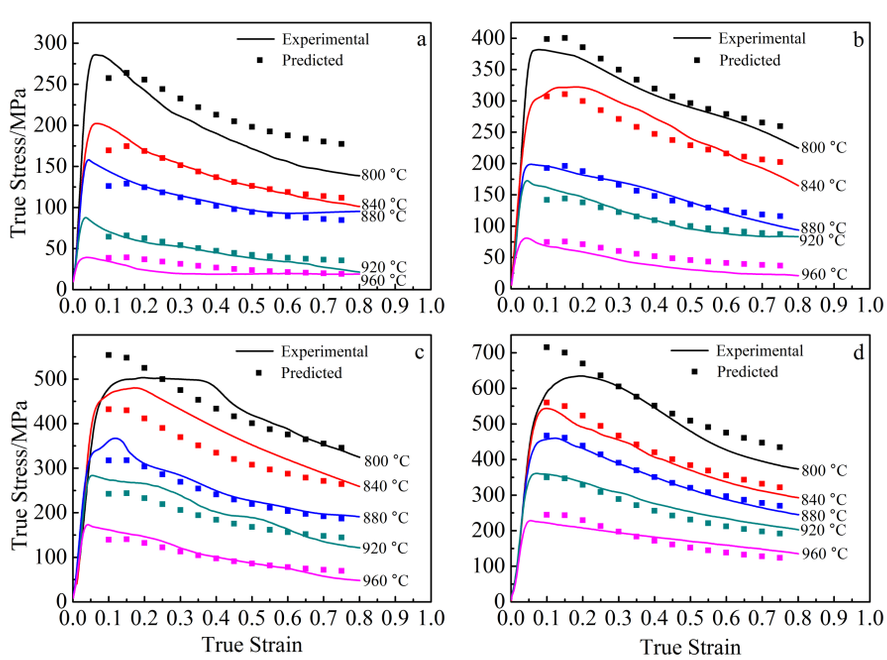

Fig.7 Comparison between the precited stresses by HS model and experimental stresses: (a) 10^{-3} s^{-1}, (b) 10^{-2} s^{-1}, (c) 10^{-1} s^{-1}, and (d) 1 s^{-1}

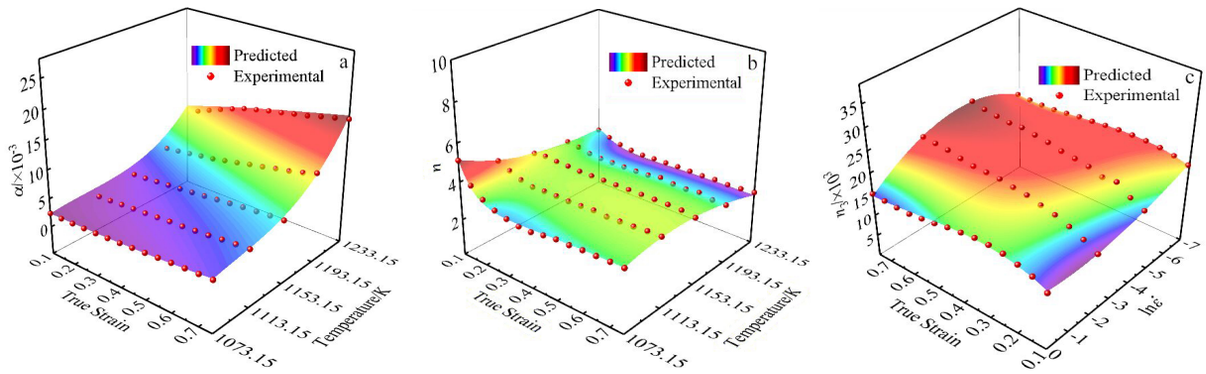

Fig.8 Relationship between α (a), n (b), and n_3 (c) and deformation temperatures, strain rates, and strain

$$\begin{cases} \alpha(\varepsilon,T) = F_0 + F_1\varepsilon + F_2T + F_3\varepsilon^2 + F_4T^2 + F_5\varepsilon^3 + F_6T^3 + F_7\varepsilon T + F_8\varepsilon^2T + F_9\varepsilon T^2 \\ n(\varepsilon,T) = \begin{bmatrix} G_0 + G_1\ln\varepsilon + G_2\ln T + G_3(\ln\varepsilon)^2 \\ +G_4(\ln T)^2 + G_5(\ln\varepsilon)^3 + G_6(\ln T)^3 \\ +G_7(\ln\varepsilon)(\ln T) + G_8(\ln\varepsilon)^2(\ln T) \\ +G_9(\ln\varepsilon)(\ln T)^2 \end{bmatrix} / \left[G_{10}\varepsilon T\right] + G_{11} \\ n_3(\dot{\varepsilon},T) = H_0 + H_1\dot{\varepsilon} + H_2T + H_3\dot{\varepsilon}^2 + H_4T^2 + H_5\dot{\varepsilon}^3 + H_6T^3 + H_7\dot{\varepsilon}T + H_8\dot{\varepsilon}^2T + H_9\dot{\varepsilon}T^2 \end{cases} \quad (15)$$

3.4 Accuracy evaluation of constitutive models

Three kinds of original strain-compensation Arrhenius constitutive model (OSCA), Hensel-Spittel constitutive model (HS) and modified Arrhenius constitutive model (MA) are established to describe the thermal deformation behavior of Ti600 alloy. The flow stresses predicted by three models and the measured stresses are compared in Fig. 10. It can be confirmed that the stress distribution of the OSCA model and HS model is relatively discrete. However, the stress distribution by the MA model is convergent and the flow stresses are uniformly distributed on one line.

Table 3 Coefficients of the binary polynomial

α	n	n_3
F_0=-5013.222	G_0=2.309×10^6	H_0=10.173
F_1=269.228	G_1=2.069×10^6	H_1=47.449
F_2=13.501	G_2=-3.663×10^5	H_2=1.335
F_3=34.944	G_3=-3991.929	H_3=-99.622
F_4=-0.012	G_4=-35693.922	H_4=0.384
F_5=2.437	G_5=-293.073	H_5=59.126
F_6=3.628×10^6	G_6=5827.749	H_6=0.00984
F_7=-0.537	G_7=-5.886×10^5	H_7=-5.9067
F_8=-0.033	G_8=279.809	H_8=-1.865
F_9=0.00027	G_9=41759.283	H_9=-1.095
	G_{10}=-0.704	
	G_{11}=-3.594	

The average absolute relative error (AARE) and correlation coefficient (R) of each model can be computed through Eq. (16) and Eq. (17) to quantitatively assess the prediction accuracy of each model.

$$\text{AARE} = \frac{1}{N}\sum_{i=1}^{N}\left|\frac{Y_i - X_i}{Y_i}\right| \times 100\% \quad (16)$$

$$R = \frac{\sum_{i=1}^{N}(X_i - \bar{X})(Y_i - \bar{Y})}{\sqrt{\sum_{i=1}^{N}(X_i - \bar{X})^2\sum_{i=1}^{N}(Y_i - \bar{Y})^2}} \quad (17)$$

where Y is the experimental stress, X is the predicted stress, and $\bar{X}$ and $\bar{Y}$ represent average value of predicted and measured flow stress, respectively.

Here, the R reflects linear correlation between predicted results and measured data. And the AARE reveals the deviation degree of predicted stress from experimental stress. The R values of OSCA model, HS model, and MA model are 0.965, 0.989, and 0.997, and the AARE values of the three models are 12.86%, 9.74%, and 3.26%. Among three models, the MA model has the largest R value and the smallest AARE value, which indicates that the MA model has the highest prediction accuracy for the Ti600 alloy.

The above constitutive models are proposed based on mathematical parameters. However, the softening mechanisms of metals may change under different deformation conditions during the hot deformation. Therefore, there may be an appropriate deviation between the flow stress predicted by the above constitutive models and the experimentally measured stress. Through the accuracy evaluation, the accuracy of the three models is within the controllable range, which means that these constitutive models can predict the hot deformation behavior of Ti600 alloy.

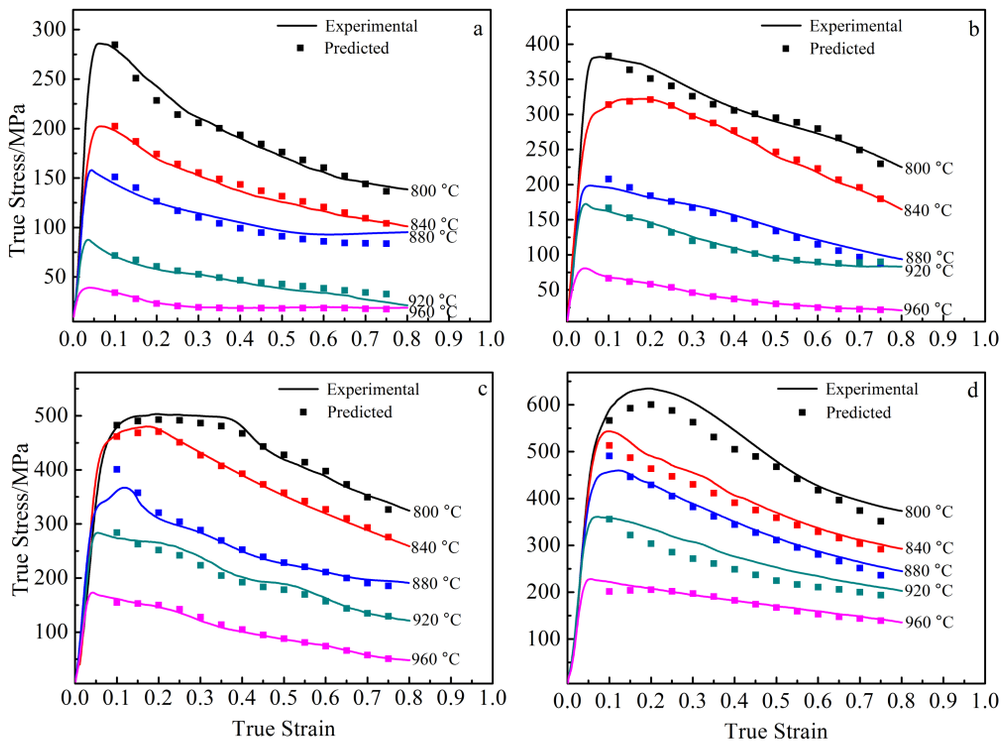

Fig.9 Comparison between the predicted stresses by MA model and experimental stresses: (a) 10^{-3} s^{-1}, (b) 10^{-2} s^{-1}, (c) 10^{-1} s^{-1}, and (d) 1 s^{-1}

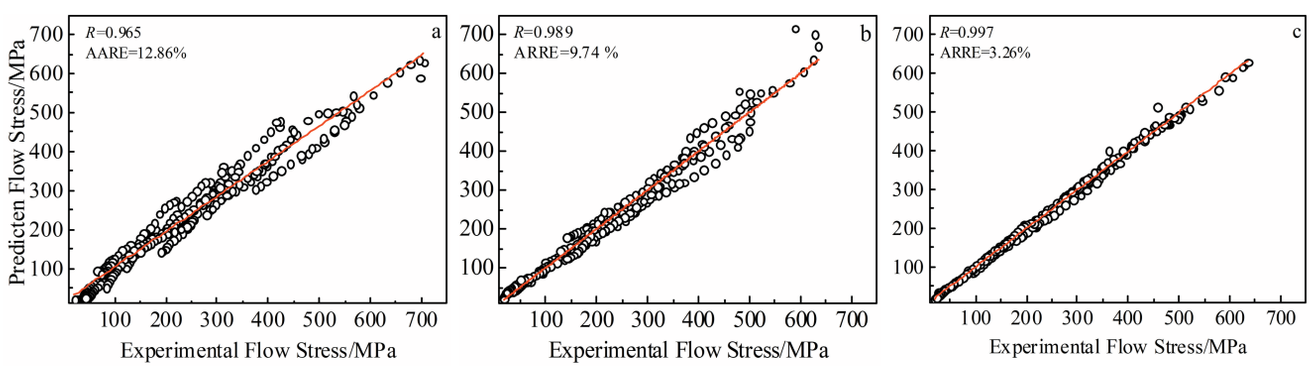

Fig.10 Comparison between experimental stresses and predicted stresses: (a) OSCA model, (b) HS model, and (c) MA model

4 Conclusions

1) The thermal deformation behavior of Ti600 alloy is significantly influenced by the strain, deformation temperatures and strain rates. The increased strain rates and decreased deformation temperatures can result in an elevated flow stress.

2) After the peak strain, the *n*-value of all curves gradually decreases due to the dynamic softening. Moreover, it can be deduced that the dynamic softening rate increases with the increase of strain rate through observing the curve slope of strain hardening exponent. And the flow softening behavior of Ti600 alloy is mainly resulted from the bending, fragmentation, DRV and DRX of α phase according to microstructure observation.

3) The OSCA model, HS model and MA model are conducted to describe the hot deformation flow properties of Ti600 alloy. Among these models, the MA model has the highest prediction accuracy, which considers the simultaneous influences of strain, temperatures and strain rates.

References

1 Lin Y, Huang J, Li H B *et al*. *Vacuum*[J], 2018, 157: 83

2 Lin Y, Wu F, Wang Q W, Chen D D *et al*. *Vacuum*[J], 2018, 151: 283

3 Ebied S, Hamada A, Borek W *et al*. *Materials Characterization* [J], 2018, 139: 176

4 Wan Z Z, Sun Y, Hu L X *et al*. *Materials Characterization*[J],

2017, 130: 25
5 Chuan W, Liang H. *Vacuum*[J], 2018, 156: 384
6 Cai Z M, Ji H C, Pei W C *et al*. *Vacuum*[J], 2019, 165: 324
7 Long S, Xia Y F, Wang P *et al*. *Journal of Alloys and Compounds* [J], 2019, 796: 65
8 Wang H R, Zhang Z Y, Zhai R X *et al*. *Materials Today*[J], 2020, 24: 101 000
9 Yang J L, Wang G F, Jiao X Y *et al*. *Materials Characterization* [J], 2018, 137: 170
10 Lei J, Zhu W G, Chen L *et al*. *Materials Today*[J], 2020, 23: 100 873
11 Wan P, Wang K L, Zou H *et al*. *Journal of Alloys and Compounds*[J], 2019, 777: 812
12 Dai Q S, Deng Y L, Tang J G *et al*. *Transactions of Nonferrous Metals Society of China*[J], 2019, 29: 2252
13 Quan G Z, Liu J, Mao A *et al*. *High Temperature Materials and Processes*[J], 2015, 34: 643
14 Saravanan L, Senthilvelan T *et al*. *Journal of Materials Research and Technology*[J], 2016, 5: 21
15 Li K, Chen Z Y, Chen T *et al*. *Journal of Alloys and Compounds* [J], 2019, 792: 894
16 Shalbafi M, Roumina R, Mahmudi R. *Journal of Alloys and Compounds*[J], 2017, 696: 1269
17 Yang Y, Peng X D, Ren F J *et al Journal of Materials Science and Technology*[J], 2016, 32: 1289
18 Detrois M, Antonov S, Tin S *et al Materials Characterization*[J], 2019, 157: 109 915
19 Lin Y C, He M, Chen M S *et al*. *Transactions of Nonferrous Metals Society of China*[J], 2016, 26: 107
20 Etaati A, Dehghani K. *Materials Chemistry and Physics*[J], 2013, 140: 208
21 Etaati A, Dehghani K, Ebrahimi G R *et al*. *Metals and Materials International*[J], 2013, 19: 5
22 Li H Y, Li Y H, Wang X F *et al*. *Materials and Design*[J], 2013, 49: 493
23 Mishra M, Balasundar I, Rao A *et al*. *Journal of Materials Engineering and Performance*[J], 2017, 26: 802
24 Bobbili R, Ramudu B V, Madhu V *et al*. *Journal of Alloys and Compounds*[J], 2017, 696: 295
25 Haghdadi N, Martin D, Hodgson P. *Materials and Design*[J], 2016, 106: 420
26 Bobbili R, Madhu V. *Materials Science and Engineering A*[J], 2017, 700: 82
27 Li H P, He L F, Zhao G Q *et al Materials Science and Engineering A*[J], 2013, 580: 330
28 Jia W T, Xu S, Le Q C *et al*. *Materials and Design*[J], 2016, 106: 120
29 Sani S A, Ebrahimi G R, Vafaeenezhad H *et al*. *Journal of Alloys and Compounds*[J], 2018, 6: 134
30 Zhao J W, Ding H, Zhao W J *et al Computational Materials Science*[J], 2014, 92: 47
31 He D G, Lin Y C, Jiang X Y *et al*. *Materials and Design*[J], 2018, 156: 262
32 Chen F, Wang H, Zhu H J *et al*. *Journal of Manufacturing Processes*[J], 2019, 38: 223
33 Wu S W, Zhou X G, Cao G M *et al*. *Materials and Design*[J], 2017, 116: 676
34 Luo J, Li M Q, Yu W X *et al*. *Materials and Design*[J], 2010, 31: 741
35 Ning Y Q, Xie B C, Liang H Q *et al*. *Materials and Design*[J], 2015, 71: 68
36 Chen X M, Lin Y C, Wen D X *et al*. *Materials and Design*[J], 2014, 57: 568
37 Mirzadeh H. *Mechanics of Materials*[J], 2015, 85: 66
38 Gavard L, Montheillet F, Coze J L. *Materials Transactions, JIM* [J], 2007, 41: 113
39 Li L, Wang Y, Li H *et al*. *Computation Materials Science*[J], 2019, 166: 221
40 Mehtedi M E, Musharavati F, Spigarelli S. *Materials and Design* [J], 2014, 54: 869

Ti600合金在(α+β)相区的热变形行为和本构模型

李会明[1,2]，张菁丽[2]，毛小南[2]，洪　权[2]，张永强[2]，潘　浩[2]，蔡建华[2]
(1. 东北大学，辽宁 沈阳 110819)
(2. 西北有色金属研究院，陕西 西安 710016)

摘　要：对具有片层状初始组织的Ti600合金的热变形行为进行了研究。变形温度范围为800~960 ℃，应变速率范围为10^{-3}~1 s^{-1}。随后提出了应变硬化指数（n）来表征流动软化和加工硬化之间的竞争。并且通过分析流变曲线和观察显微组织研究了该合金的软化行为。结果表明，变形参数对Ti600合金的流变行为有显著影响。当变形超过峰值应变之后，n值逐渐降低，动态软化过程开始占主导地位。微观组织分析表明：热变形过程中，α相的弯曲、破碎、动态回复和动态再结晶行为是造成Ti600合金软化的主要原因。最后基于实验数据，建立了3种本构模型，分别是应变补偿Arrhenius模型、Hensel-Spittel模型和修正的Arrhenius模型，来表征Ti600合金的流变行为。将3种模型预测的流变应力与实验结果进行比较，并计算其相关系数值和平均相对误差值来评估模型的准确性。3种模型的相关系数值分别为0.965、0.989和0.997，平均相对误差值分别为12.86%，9.74%和3.26%。这些结果表明，这3种模型都可以描述Ti600合金的流变行为，而修正的Arrhenius模型具有最高的预测精度。

关键词：Ti600合金；热压缩；变形行为；软化行为；本构模型

作者简介：李会明，男，1996年生，硕士生，东北大学材料科学与工程学院，辽宁 沈阳 110819，电话：029-86250729，E-mail：lihuiming3481@126.com